Not just fractal surfaces, but surface fractal aggregates: Derivation of the expression for the structure factor and its applications

R. Besselink, T. M. Stawski, A. E. S. Van Driessche, and L. G. Benning

Citation: The Journal of Chemical Physics **145**, 211908 (2016); doi: 10.1063/1.4960953
View online: http://dx.doi.org/10.1063/1.4960953
View Table of Contents: http://scitation.aip.org/content/aip/journal/jcp/145/21?ver=pdfcov
Published by the AIP Publishing

Not just fractal surfaces, but surface fractal aggregates: Derivation of the expression for the structure factor and its applications

R. Besselink,[1,a),b)] T. M. Stawski,[1,2,a),b)] A. E. S. Van Driessche,[3] and L. G. Benning[1,2]
[1]*German Research Centre for Geosciences, GFZ, 14473 Potsdam, Germany*
[2]*Cohen Geochemistry, School of Earth and Environment, University of Leeds, LS2 9JT Leeds, United Kingdom*
[3]*Université Grenoble Alpes, CNRS, ISTerre, F-38000 Grenoble, France*

(Received 2 June 2016; accepted 1 August 2016; published online 17 August 2016)

Densely packed surface fractal aggregates form in systems with high local volume fractions of particles with very short diffusion lengths, which effectively means that particles have little space to move. However, there are no prior mathematical models, which would describe scattering from such surface fractal aggregates and which would allow the subdivision between inter- and intraparticle interferences of such aggregates. Here, we show that by including a form factor function of the primary particles building the aggregate, a finite size of the surface fractal interfacial sub-surfaces can be derived from a structure factor term. This formalism allows us to define both a finite specific surface area for fractal aggregates and the fraction of particle interfacial sub-surfaces at the perimeter of an aggregate. The derived surface fractal model is validated by comparing it with an *ab initio* approach that involves the generation of a "brick-in-a-wall" *von Koch* type contour fractals. Moreover, we show that this approach explains observed scattering intensities from *in situ* experiments that followed gypsum ($CaSO_4{\cdot}2H_2O$) precipitation from highly supersaturated solutions. Our model of densely packed "brick-in-a-wall" surface fractal aggregates may well be the key precursor step in the formation of several types of mosaic- and meso-crystals. [http://dx.doi.org/10.1063/1.4960953]

INTRODUCTION

In colloid sciences fractal scaling concepts constitute an important formalism that provides for the statistical description of the properties of particles and their aggregates (e.g., morphologies, porosity, density, and specific surface area). The fractal nature of colloids can be experimentally quantified using scattering techniques, and based on a combination of theoretical and experimental evidence[1–18] two distinct scaling laws have been used to describe experimental observations: mass fractals and surface fractals. Mass fractal scaling can be associated with the packing efficiency of an aggregate, which in turn depends on the type of aggregation, e.g., diffusion or reaction limited mechanism.[13–21] On the other hand, surface fractal scaling only relates to the perimeter of a particle or aggregate of particles and correlates with its specific surface area.[1–5]

The core idea behind mass fractals stems from our need to statistically describe aggregation processes involving primary particles. To exemplify this, we will assume for simplicity that a system only has spherical and monodisperse particles with radii r_0. These particles aggregate into larger structures, whose size is typically characterized by a radius of gyration R_g (see Fig. 1(a)). For a mass fractal aggregate, the average number of particles $N(r)$ within a distance of a variable length scale r, with an arbitrary origin within the aggregate ($r < 2R_g$), is given by[10,11]

$$N(r) \propto \left(\frac{r}{r_0}\right)^{D_m}, \tag{1}$$

where D_m is a mass fractal dimension, which in a three-dimensional space can assume values of $1 \leq D_m < 3$. Regular objects such as a thin rod, a thin plate, or a cube have an integer D_m of 1, 2, and 3, respectively. However, for more complex morphologies, such as branched objects, $N(r)$ does not necessarily scale with an integer value of D_m, depending on the aggregate packing density, D_m can have any fractional value between 1 and 3. For particles aggregating in solution, one would expect mass fractals, because such structures usually form at relatively low local particle concentrations and considerably large diffusion lengths.[15–21] This fact is exemplified by the common observation of such aggregates in nature. Important to note is that the mathematical formalism used for describing these structures is well established.[8–12]

On the other hand, for surface fractal aggregates the current concepts do not explicitly consider primary particles as building blocks for the aggregates, since their surface fractal dimensions cannot be associated with the internal packing efficiency of primary particles. This is because, surface fractal scaling deals with an apparently dense object whose surface area, α, scales with the variable length scale r as follows:[3]

$$\alpha(r) = \alpha_2\left(\frac{r}{l_2}\right)^{2-D_s}, \tag{2}$$

a)Authors to whom correspondence should be addressed. Electronic addresses: rogier@gfz-potsdam.de and stawski@gfz-potsdam.de.
b)R. Besselink and T. M. Stawski contributed equally to this work.

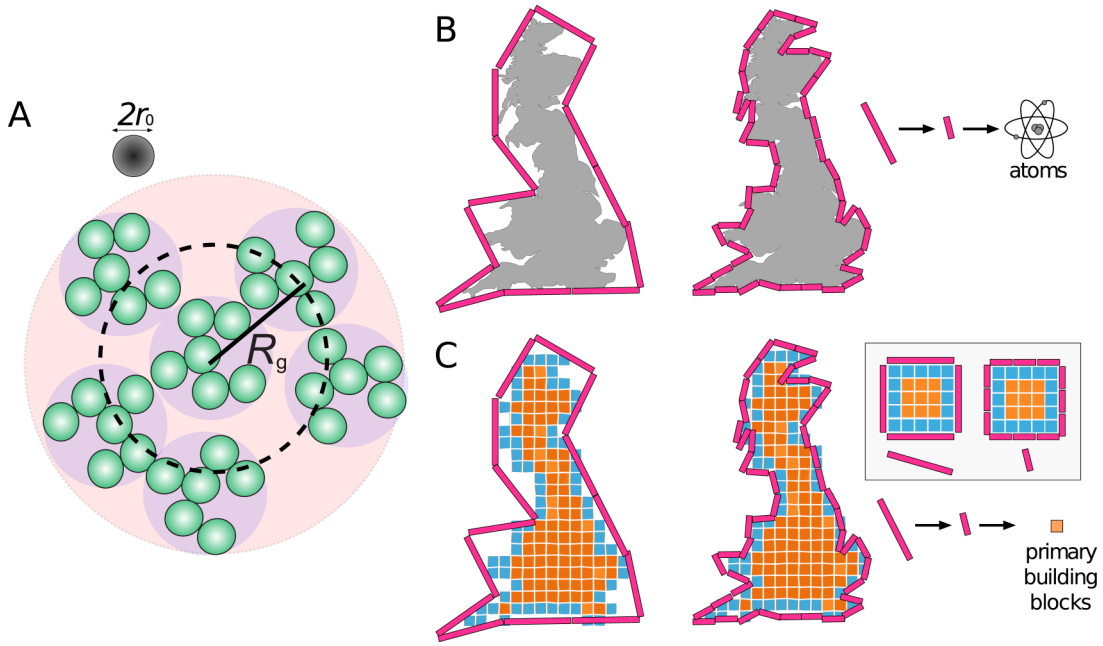

FIG. 1. (a) Mass fractal aggregate characterized by a radius of gyration R_g and composed of spherical primary particles of radii r_0 (grey and green spheres); (b) Mandelbrot's[22] "How long is the coast of Britain?" example illustrates that the total measured length of the coast (i.e., fractal contour) increases with decreasing size of the yardstick (pink line). When the yardstick is in relative terms infinitely small (or at least smaller than the smallest d-spacing corresponding to a measured q-range in scattering, e.g., atomic), the total length of a fractal contour will become effectively infinite; (c) in analogy to (b) the concept of the surface fractal aggregate is based on the total length of the coastline still being a fractal, but with a yardstick that has a practical finite size. This finite size can be associated with the size of the primary building blocks (orange and blue squares) making up the entire object. As a consequence, the length of the contour becomes finite. The blue squares represent the building blocks at the surface. The inset in (c) depicts a rectangular island composed of primary building blocks, which is an analogue of an aggregate with a smooth surface ($D_s = 2$). Because of its flat shape, the measured length of the contour line is independent of the length of the yardstick, provided that the yardstick is considerably shorter than the measured length.

where α_2 is the projected area of a rough surface onto a 2D plane (i.e., area of the "*en face* photo" of a rough surface), D_s is the surface fractal dimension, and l_2 is the limiting length-scale, which is related to the size of the discrete building blocks (e.g., atoms, primary particles, etc.). Such surface fractal dimensions can assume values between $2 \leq D_s < 3$, where $D_s = 2$ represents a perfectly smooth surface, and values approaching 3 represent a "very rough" surface. The concept of surface fractals is in line with a classical paper by Mandelbrot,[22] which showed that the apparent length of Britain's coastline (i.e., contour line) depends on the length of the applied yardstick (see Fig. 1(b)). Although the example used by Mandelbrot dealt with two-dimensional objects, and thus the yardsticks and the fractal properties were one-dimensional, in surface fractals we consider the surfaces of three-dimensional objects. Consequently, the yardsticks and fractal properties are two-dimensional, and thus a yardstick can be linked to the surface area α described in Eq. (2). Although the surface fractal formalism does not exclude the existence of primary particles (i.e., larger than a single atom) making up the surface of the aggregate, it is typically assumed that surface fractal scaling extends to the infinitely small "atomic" level and hence $r \rightarrow 0$ (in analogy to Fig. 1(b)). In such a case, this type of scaling is attributed to the properties of surfaces (regardless if these are surfaces of amorphous particles[23] or external crystal surfaces[24]), excluding smaller particle morphologies.

There is still an open question, whether we can rationalise the physicochemical process(es) leading to the formation of true surface fractal aggregates. Such surface fractals would have to be internally (nearly) close-packed; however, the primary building blocks making up such an aggregate still has to be distinguishable from their surroundings. This means that they have to be separated by low-density spacers (e.g., Fig. 1(c)). The presence of such spacers seems to contradict the close-packing hypothesis; however, close-packing only requires a high coordination number of nearest neighbours. Kolb and Herrmann[25] showed through Monte Carlo simulations of highly concentrated colloidal aggregates, that if the "local" concentration of particles is close to 1 (i.e., the particles have very little space to move), then surface fractal aggregates are formed instead of their mass counterparts.[25] This is particularly relevant if we consider that recent studies have pointed out that, for example, nucleation is driven by local density fluctuations,[26,27] and that due to these fluctuations the local particle concentration can significantly increase resulting in much decreased diffusion lengths. In a recent work[28] we showed that, during the formation of gypsum ($CaSO_4 \cdot 2H_2O$), surface fractal aggregates made of sub-3 nm primary species constituted a crucial step in the process, without which nucleation nor further growth could proceed. This insight was gained from experimental *in situ* and time-resolved scattering evidence and showed that the appearance of surface fractal aggregates was indeed preceded by the formation of domains of increased local number density of the primary species. We attributed the onset of aggregation to the "collapse" of these high-density domains and the sudden increase in the local volume fractions of primary

species. As a result, surface fractal aggregates formed, yet we could still distinguish the primary particles making up these larger morphologies. In addition, this surface fractal aggregate concept could be particularly relevant within the framework of non-classical crystallization models, which suggest that crystals may form as a result of aggregation of primary particles. As such, this concept could be associated, if not actually considered as interchangeable, with the notion of meso-crystals defined for the growth by oriented attachment of nanoparticles building up single crystals.[29] It also appears that a surface fractal aggregate model could explain various aspects of the concept of mosaicity that characterises the formation of inorganic[30–32] and macromolecular[33–36] single crystals.

In the aforementioned study on the $CaSO_4$ system, we used small-angle X-ray scattering data to draft the concept of surface fractal aggregation. Scattering approaches are among the most powerful experimental tools for *in situ* and time-resolved characterization of nano- and microscopic properties of colloidal systems, including their possible fractal nature and aggregation mechanism. Nevertheless, the prime conceptual missing link between mass fractal and surface fractal systems has been the total lack of any suitable mathematical model that describes the measured scattering phenomena for surface fractal aggregates. To fill this gap, we derived, validated, and tested an advanced mathematical model in this work, which allowed us to analyse and fit scattering data, and explained the concepts of surface fractal aggregates for colloidal systems.

SCATTERING FROM FRACTAL OBJECTS

Both mass and surface fractals are relatively easy to observe in the small-angle scattering region of electromagnetic waves. For mass fractals, the isotropic scattering intensity I can be expressed as a function of the modulus of the scattering vector q, for a certain range of length-scales (defined by q) as follows:

$$I(q) \propto q^{-D_m}, \tag{3}$$

whereas, for surface fractals,

$$I(q) \propto q^{-6+D_s} \tag{4}$$

applies.

To categorize a structure as a true fractal, these dependencies should extend for at least one decade in q, and the $\log I(q)$ *vs.* $\log q$ representation should yield a characteristic straight line for both types of fractals (Fig. 2). If the exponent (i.e., the slope in the logarithmic representation) is <-1 and >-3, then it corresponds to $-D_m$, and we deal with mass fractals (Eq. (3); lines I and II in Fig. 2). On the other hand, if the exponent is <-3 and >-4, then it is equal to $-6 + D_s$, and we should consider surface fractals (Eq. (4); lines III and IV in Fig. 2). This constitutes in many cases a straightforward method to establish the occurrence, and distinguish between the two types, of fractal structures in a system (Fig. 2).

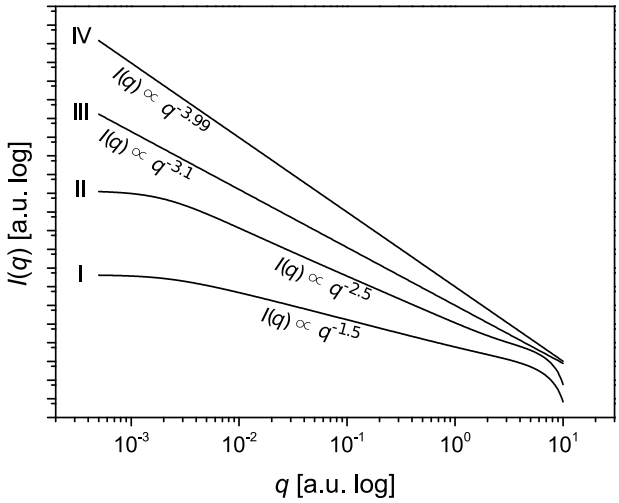

FIG. 2. $\log I(q)$ *vs.* $\log q$ representation of simulated scattering intensities: (I) exponent −1.5 for $\sim 0.01 < q < \sim 2$ a.u. indicates a lower density mass fractal of $D_m = 1.5$; (II) exponent −2.5 for $\sim 0.01 < q < \sim 2$ a.u. indicates a higher density mass fractal of $D_m = 2.5$; (III) exponent −3.1 for the entire q-range indicates a rough surface fractal of $D_s = 6 - 3.1 = 2.9$; (II) exponent −3.99 for the entire q-range indicates an almost smooth surface fractal of $D_s = 6 - 3.99 = 2.01$.

Scattering from mass fractal aggregates of primary particles

Following the above defined notions, it becomes clear that in Fig. 2, within the region spanning $\sim 0.01 < q < \sim 2$ a.u., the curves I and II originate from mass fractal structures. However, the power law q^{-D_m} relationship holds neither for $q < \sim 0.01$ a.u. in the low-q regime where the curves flatten out approaching q^0 nor for $q > \sim 2$ a.u. where the exponents sharply increase at high-q. The low-q regime marks the characteristic size of an entire aggregate with a given R_g (e.g., Fig. 1(a)). Conversely, the high-q regime contains information about the individual primary particles of radius r, which make up the aggregate. This regime also contains information about the size, shape, and/or polydispersity of the primary particles. The scattering intensity from such a system with both individual primary particles and aggregates can be expressed as the product of the three major components[10,11]

$$I(q) = v_{pp}\phi(\Delta\rho)^2 \cdot P(q) \cdot S(q), \tag{5}$$

where the first contribution is described by $v_{pp}\phi(\Delta\rho)^2$, which is the scattering pre-factor, in which v_{pp} denotes the volume of a primary particle, ϕ is the total volume fraction of the primary particles in the matrix, and $\Delta\rho$ is the scattering length density difference between the primary particles and the surrounding homogenous matrix (e.g., solvent). The other two components are the functions, $P(q)$ and $S(q)$, which describe the form and structure of the particles, respectively. $P(q)$ originates from intraparticle interferences and defines the geometrical properties of the primary particles building the aggregate (and thus also defines v_{pp}). The contributions of $P(q)$ in curves I and II in Fig. 2 are visible at $q > \sim 2$ a.u. On the other hand, $S(q)$ originates from interparticle interferences and describes the geometrical arrangement of the primary particles. This function describes the $q < \sim 2$ a.u. features of the scattering patterns in curves I and II in Fig. 2.

For mass fractals the contributions of the various length-scales are distinguishable in the scattering pattern, expressed by Eq. (5), and can be easily separated. For an in-depth description we refer the reader to the literature.[12,37,38] Nevertheless, for the sake of a good understanding of the model for surface fractals we develop below, we will briefly explain here these concepts.

Firstly, for simplicity, we consider a monodisperse system with spheres of radius r_0. Hence, $P(q)$ is given/known, and it is by default normalized to its primary particle volume and consequently $P(q \to 0) = 1$. Furthermore, $S(q)$, once normalized in such a way that $S(q \to \infty) = 1$, can be expressed as[10,11,39,40]

$$S(q) = 1 - \frac{V_2(q)}{v_1} = 1 + \frac{1}{v_1} 4\pi \int_0^\infty (g(r) - 1) r^2 \frac{\sin qr}{qr} \mathrm{d}r, \tag{6}$$

where V_2 represents the perturbed or excluded particle volume, which represents the length-scale dependent volume that will not be occupied by primary particles. v_1 is the average available volume per primary particle and equates to V/N_1, where V is the sample's scattering volume and N_1 the total number of primary particles.[40] v_1 is therefore the inverse of the particle number density n_1. The mass fractal scaling in Eq. (6) is represented by $g(r)$. This is a correlation function that describes the probability of finding two locations separated by a distance r, which in the case of mass fractals is proportional to the amount of volume occupied by solid matter, $V(r) \propto r^{D_\mathrm{m}}$. Using the formalism defined by Chen and Teixeira[10,11] the correlation function for the total number of particles $N(r)$ within a sphere of radius r is defined by the expression

$$\begin{aligned} n_1 \cdot (g(r) - 1) &= \frac{1}{4\pi r^2} \cdot \frac{\mathrm{d}N(r)}{\mathrm{d}r} = \frac{1}{4\pi r^2} \cdot \frac{\mathrm{d}}{\mathrm{d}r} \left(\frac{r}{r_0} \right)^{D_\mathrm{m}} \\ &= \frac{D_\mathrm{m}}{4\pi} \cdot \frac{r^{(D_\mathrm{m}-3)}}{r_0^{D_\mathrm{m}}}, \end{aligned} \tag{7}$$

where n_1 is the overall particle number density within the sample's scattering volume V (i.e., V represents the sample volume that is exposed to incident beam). A finite size of aggregates can be taken into account in the expression for $g(r)$ by multiplying Eq. (7) by an exponential cut-off function[8–12] $\exp(-r/\xi)$, where ξ is the cut-off length. This length marks the perimeter of the aggregate, and it can be related to R_g from Eq. (1).[10,11] It is worth noting that, by including the exponential cut-off function (Eq. (7)), n_1 represents a local particle number density within the boundary of the mass-fractal aggregate rather than an overall particle number density. By substitution of a normalized correlation function for mass fractals (as in Eq. (7)) and including a multiplied exponential cut-off function, $\exp(-r/\xi)$, within the normalized definition of the structure function (Eq. (6)) the following structure function for mass-fractal aggregates is derived:[10,11]

$$S_\mathrm{MF}(q) = 1 + \frac{D_\mathrm{m}\Gamma(D_\mathrm{m} - 1)}{(qr_0)^{D_\mathrm{m}}} \cdot \frac{\sin[(D_\mathrm{m} - 1)\mathrm{atan}(q\xi)]}{\left(1 + (q\xi)^{-2}\right)^{(D_\mathrm{m}-1)/2}}, \tag{8}$$

where Γ denotes a gamma function.

This mass fractal structure factor, $S_\mathrm{MF}(q)$, is dimensionless and normalized by its primary particle volume, and the structure factor goes to unity in the high-q limit ($S(q \to \infty) = 1$). Hence, this formalism enables the inclusion of a separate form factor that can describe the shape of the primary entities. Consequently, this approach provides information about both the average number of primary particles per aggregate and the size of the primary entities, which in turn correlates with the specific surface area and porosity of the aggregates.

Model development for surface fractal structures

Based on a similar approach as for the mass fractal structure factor, below we derive a surface fractal structure factor that will then be linked to, and validated with, our scattering data. To do this, we start with the advanced expressions for scattering from surface fractal morphologies derived by Bale and Schmidt,[1] Reich *et al.*,[2] and Wong and Bray,[3,4]

$$I(q) = A \cdot \frac{\Gamma(5 - D_\mathrm{s}) \sin[\pi(3 - D_\mathrm{s})/2]}{3 - D_\mathrm{s}} \cdot q^{-6+D_\mathrm{s}}, \tag{9}$$

where A is a constant proportional to the surface area of the scattering features (e.g., a particle, crystal or pore surface, etc.) and the scattering contrast.

Contrary to Chen and Teixeira's derivation(s) for the mass fractal structure factor (Eq. (8)), the scattering intensity function for surface fractals in Eq. (9) was not normalized against the primary particle volume (Eq. (6)), and hence Eq. (9) does not describe a structure factor function. Consequently, it cannot be used to describe a multi-level hierarchical structure composed of primary particles that assemble into larger aggregates. With Eq. (9), we can simulate various scattering patterns representing surface fractals (as shown in the $\log I(q)$ *vs.* $\log q$ in Fig. 2, curves III and IV). In this representation, the simulated scattering patterns turn into simple straight lines, which essentially lack any characteristic features at both extremes of the limiting q-range (compared to curves I and II for mass fractals). Hence, in the current form Eq. (9) does not describe surface fractal aggregates, but merely fractal rough surfaces.

To include a form factor, we start with the established model of fractal surfaces, which relies on a first order approximation of the correlation function for the scattering intensity,[40,41] that can be expressed as

$$\left(\frac{d}{dr} g(r) \right)_{r \to 0} = \frac{-1}{4(1 - \phi)} \cdot \frac{\alpha}{V\phi}, \tag{10}$$

where V is the sample's scattering volume, α is the surface area of the solid and as introduced above in Eq. (2), and ϕ is the total volume fraction of the primary particles within the sample's scattering volume. For fractal rough surfaces, the surface area α depends on the limiting length-scale, l_2, introduced in Eq. (2). Now, let us assume that a fractal rough surface is composed of small spherical subunits of radius r_0 (see Figs. 3 and 1(c)). In such a case the limiting length-scale of the surface roughness will be approximately the same size as that of the primary particles that make up the rough fractal surface (i.e., $l_2 \sim 2r_0$). Furthermore, when a solid aggregate is built of N_pp number of spherical primary particles, the

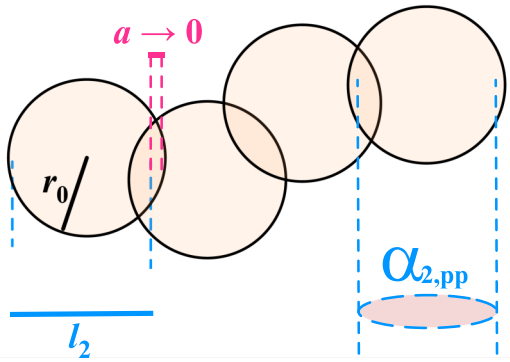

FIG. 3. Schematic representation of the characteristic length-scales considered for a fractal surface composed of spherical primary particles of radii r_0. l_2 is a limiting length-scale and $l_2 = 2r_0 - a$, where a is a small overlap parameter and $a \to 0$. $\alpha_{2,pp}$ is a surface area of the projection of a single spherical primary particle.

total volume of the resulting solid phase within the aggregate (i.e., $V\phi$: a product of the sample's scattering volume V and a total volume fraction of primary particles ϕ) can be described by Eq. (11) and is illustrated in Fig. 3,

$$\phi V = N_{pp} \cdot {}^4/_3\,\pi r_0^3. \tag{11}$$

For a typical aggregate, only a limited number of primary particles $N_{b,pp}$ are located at the rough boundary surface ($N_{b,pp} \ll N_{pp}$). Furthermore, as postulated by Wong and Bray,[3] primary particles can be partially merged together, and thus to some extent they may overlap (*a la* Minkowski sausage[3]). For the sake of simplicity we assume that the overlap, a, is negligibly small compared to the particle radius and thus $l_2 = 2r_0$. In our derivation, $\alpha_{2,pp}$ denotes the surface area of the projection of a single primary particle (Fig. 1(a), grey and green spheres), and thus the total projected surface area of the so formed aggregate can be expressed as

$$\alpha_2 = N_{b,pp}\alpha_{2,pp} = N_{b,pp} \cdot \pi(l_2/2)^2 = N_{b,pp} \cdot \pi r_0^2. \tag{12}$$

By combining Eqs. (10)-(12) we obtain

$$\left(\frac{d}{dr}g(r)\right)_{r\to 0} = \frac{-1}{4(1-\phi)} \cdot \frac{N_{b,pp} \cdot \pi r_0^2}{N_{pp} \cdot {}^4/_3\,\pi r_0^3} \cdot \left(\frac{r}{2r_0}\right)^{2-D_s} = \frac{-3\phi_b}{16 r_0} \cdot \left(\frac{r}{2r_0}\right)^{2-D_s}. \tag{13}$$

Here, $\phi_b = N_{b,pp}/N_{pp}$ is the fraction of primary particles located at the fractal surface boundary and for dilute systems $(1-\phi) \approx 1$. Integration of Eq. (13) by satisfying the boundary condition $g(r \to 0) = 1$ results in the following correlation function $g(r)$, which describes surface fractal aggregates:

$$g(r) = 1 - \frac{3\phi_b}{8(3-D_s)} \cdot \left(\frac{r}{2r_0}\right)^{3-D_s}. \tag{14}$$

Importantly, this new correlation function, $g(r)$, also considers smaller primary entities of size r_0. Consequently, we can substitute this correlation function into the definition of $S(q)$ in Eq. (6) and derive a new expression for the surface fractal structure factor $S_{SF}(q)$,

$$S_{SF}(q) = 1 - \int_0^\infty \frac{9 \cdot 4\pi \cdot \phi_b \cdot r^{5-D_s}}{32\pi \cdot (3-D_s)\, r_0^3 (2r_0)^{3-D_s}} \cdot \frac{\sin qr}{qr} dr = 1 + \frac{9\phi_b \Gamma(5-D_s)}{(2qr_0)^{6-D_s}} \cdot \frac{\sin[\pi(3-D_s)/2]}{3-D_s}, \tag{15}$$

where the available primary particle volume v_1 (see Eq. (6)) is approximated as the volume of a primary particle with a radius r_0.

In accordance with Wong and Bray,[3] this function is still valid for surface fractal dimensions, D_s up to 3, and the term $\sin[\pi(3-D_s)/2]/(3-D_s)$ converges to $\pi/2$. Please note that, contrary to the mass fractal equation (Eq. (8)) we did not include an upper cut-off value of the aggregate. This is only useful when all features, including the primary particle form factor, the intermediate plateau regime, the surface fractal regime, and the upper cut-off regime fall within the measured q-range. Since such aggregates are typically orders of magnitude larger as the primary particles, we assume that these aggregates extend to macroscopic sizes and consequently, $I(q \to 0) \to \infty$.

DISCUSSION

The general properties of surface fractal aggregates

Based on the mathematical concepts developed above we can now simulate the expected scattering profiles for any system as a function of the three characteristic parameters of Eq. (15), namely, ϕ_b, which is the fraction of primary particles located at the fractal surface boundary; D_s, the surface fractal dimension; and r_0, the primary particle radius. We used spherical amorphous silica particles (with a density of 2.196 g/cm^3)[46] as an example (Fig. 4). The surface fractal structure factor from Eq. (15) has to be combined with a form factor function of primary particles making up an aggregate (as expressed by Eq. (5)), for which we used a form factor for monodisperse spheres[39,40,42] with radius r_0, $P_{sphere}(q)$ (Eq. (16)). This way the three parameters of the structure factor function, $S_{SF}(q)$, can be associated with the specific surface area and the typical length-scale of surface interfacial sub-surfaces of an aggregate. In real systems, these parameters are essential, for instance, when considering the catalytic activity or adsorption efficiency of a catalyst,[43–45]

$$P_{sphere}(q) = \left(3\frac{\sin qr_0 - qr_0 \cos qr_0}{(qr_0)^3}\right)^2. \tag{16}$$

For large q-values, $P_{sphere}(q)$ from Eq. (16) will oscillate around an average value of ${}^9/_2\,(qr_0)^{-4}$ (Fig. 4(a), dark green curve I). From a mathematical standpoint such oscillations are not an issue, yet the fringes would blur the simulated scattering curves at high-q. For clarity, this spherical form function is transformed into an approximated spherical form factor function without figure-obstructing fringes ($P_{app}(q)$; Eq. (17)). When plotted in Fig. 4(a) (light green curve II) it becomes clear that this provides a good approximation for

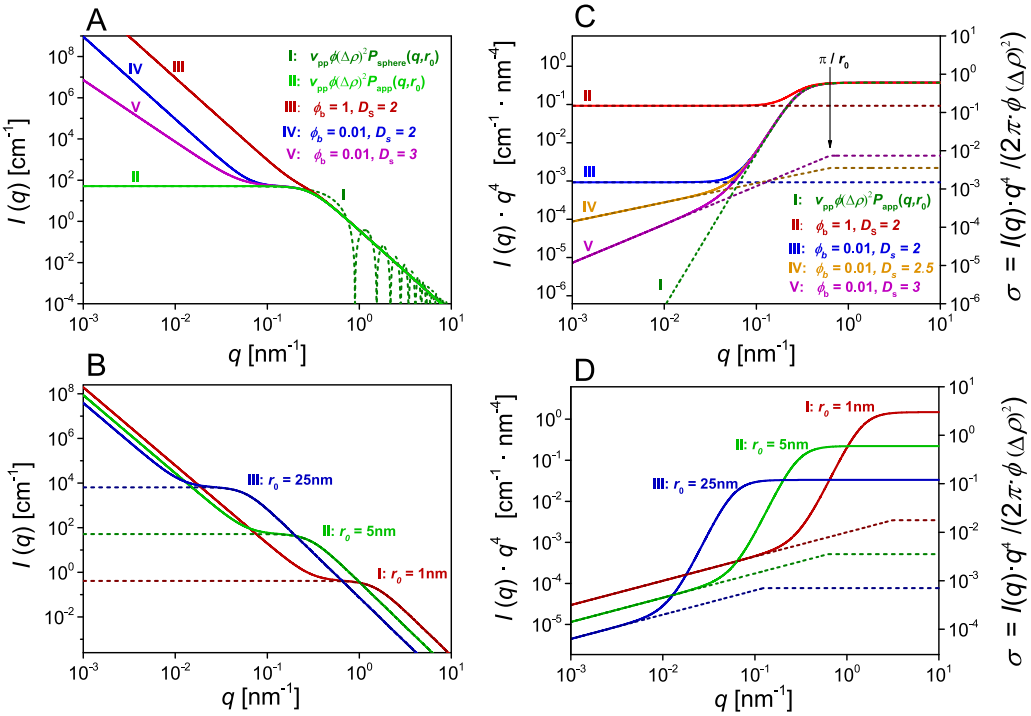

FIG. 4. Simulated scattering patterns based on Eqs. (5), (15), and (17). The volume fraction, ϕ, and the scattering contrast, $\Delta\rho$, were calculated for aqueous dispersions of amorphous silica particles of density[46] 2.196 g/cm^3 and $\phi = 0.5\%$. The scattering length density difference was calculated with respect to water. (a) log $I(q)$ *vs.* log q representation (Porod plot) for constant $r_0 = 5$ nm and various ϕ_b and D_s; (b) Porod plot for various r_0, but with constant $\phi_b = 0.01$ and $D_s = 2.5$; (c) log($I(q)\cdot q^4$) *vs.* log q plot for surface fractals based on the lines shown in (a), the secondary y-axis represents the modelled specific surface area which is proportional to the $I(q)\cdot q^4$-axis; (d) log($I(q)\cdot q^4$) *vs.* log q plot for surface fractals based on (b) with a specific surface area on the secondary axis.

$P_{sphere}(q)$,

$$P_{app}(q) = \left(\frac{1}{1 + 2/9\,(qr_0)^4}\right). \quad (17)$$

This way we can differentiate the three distinct effects that the ϕ_b, D_S, and r_0 parameters have on the scattering curves (Fig. 4):

(i) The combination of Eqs. (5), (15), and (17) reveals that the scattering intensity originating from fractal surfaces scales linearly with the fraction of particles (ϕ_b) located at this surface (e.g., blue squares in Fig. 1(c)). For instance, a 100-fold decrease in ϕ_b causes a 100-fold decrease in scattering intensity at low-q, as illustrated by curves III and IV in Fig. 4(a).

(ii) In analogy to other aforementioned surface fractal models,[1–5] the exponent of the surface fractal regime (at low-q) in a Porod plot increases from −4 to −3 when the surface fractal dimensions, D_s, shift from 2 to 3 (Fig. 4(a), curves IV and V).

(iii) The effect the primary particle radius, r_0, has on the simulated intensity patterns is shown in Fig. 4(b). The intensity value at which the form factors level off (dashed lines in Fig. 4(b)) scales proportionally with the volume of the primary particles. Furthermore, an extrapolation of the primary particle contribution to $q \to 0$ is directly equal to the scattering pre-factor $v_{pp}\phi(\Delta\rho)^2$ (see Eq. (5)). The inflection points in Fig. 4(b) (and Fig. 4(a)) divide the scattering patterns into a low-q part, dependent solely on the structure factor ($S_{SF}(q)$, Eq. (15)), and a high-q part, describable exclusively by the primary particle's form factor ($P_{app}(q)$; Eq. (17)).

The above derived surface fractal model can be used to determine the specific surfaces of the primary particles, and their aggregates, at different length-scales by using a log($I(q)\cdot q^4$) *vs.* log q representation (Fig. 4(c)). It was shown by Porod,[47] that for a high-q limit, when the scattering is described by the form factor function of only primary particles with radius r_0, the total smooth surface area of these particles (i.e., the total sum of the individual surface areas of all primary particles) is independent of the limiting length-scale for $\pi/r_0 < q < \infty$. Therefore, the obtained shapes of the curves in the high-q part are characterized by a plateau in a log($I(q)\cdot q^4$)-log q-plot for $q \to \infty$ (Fig. 4(c), curve I). The associated specific surface, σ (shown as a secondary right hand axis in Figs. 4(c) and 4(d)) is determined for this high-q limit as follows:

$$\sigma = \frac{\alpha}{V\phi} = \frac{1}{2\pi\phi(\Delta\rho)^2} \lim_{\pi/r_0 < q \to \infty} I(q)\cdot q^4. \quad (18)$$

Converting the intensity axis into a specific surface area axis (right-hand side y-axis in Figs. 4(c) and 4(d)) reveals that when smooth aggregates of primary particles are considered (e.g., particles with a $D_s = 2$ as shown in Fig. 4(c), curves II and III), the plots exhibit two plateaus. The aforementioned high-q plateau originates from the total surface of primary particles (Eq. (18)), while the 2nd low-q plateau is associated with the surface of smooth aggregates (low-q regime). In analogy to the total length of the coastline concept illustrated

in Fig. 1(c), the case of a surface fractal dimension $D_s = 2$, would correspond to a modified figure in which, instead of an irregularly shaped island, we would have an island with a very regular shape, such as the rectangle in Fig. 1(c). However, such a regularly shaped island would itself still be composed of much smaller bricks. By using such an approach, any measurement of the length of the coastline contour line (in analogy to a specific surface) with any yardstick of a length sufficiently shorter than the dimensions of our rectangular island, but longer than the dimension of the building-block brick, would yield the same result. This is analogous to a plateau in $\log(I(q)\cdot q^4)$ *vs.* $\log q$ representation (Fig. 4(c), curves II and III). In the special case of $\phi_b = 1$ and $D_s = 2$, the specific surface area of an aggregate measured this way would be exactly 4 times smaller than the specific surface area of the particles that make it up. This is because the approximated surface area of a circular smooth surface segment $\alpha_{2,pp} = \pi\cdot r_0^2$ (see Fig. 3 for clarification) is exactly 4 times smaller than the surface of a sphere $\alpha_{sphere} = 4\pi\cdot r_0^2$ (see Fig. 4(c), curve II). This statement holds under the assumption that the average electron density of the aggregate is close to the electron density of the individual primary particles. For sake of simplicity we neglected the contribution of the electron lean regions between the bricks to the electron density of the whole aggregate.

On the other hand, for $D_s > 2$, a low-q plateau is not visible in our $\log(I(q)\cdot q^4)$-$\log q$-plot. Instead, a linear region with a constant slope is observed for $q < \pi/r_0$ (Fig. 4(c), curves III and IV; Fig. 4(d)). If we return for a moment to Figs. 1(b) and 1(c), we immediately see that the specific surface (analogous to the length of a contour line) is not a constant value, because it depends on our measurement yardstick. Now let us imagine that England is composed of small bricks (Fig. 1(c)). In such a case, the length of the coastline increases for decreasing yardstick length, until the yardstick reaches the size of the primary bricks that form England. Consequently, the map of England is a fractal object only down to the size of these primary building blocks. Likewise, we can assume that the rough surface area α increases for decreasing yardstick length r, until r reaches the size of the smallest entities: $r = l_2 \approx 2r_0$ (Eq. (2) and Fig. 2). Hence, the specific surface area of a rough surface fractal aggregate, σ_{SF}, can be determined by extrapolating $I(q)\cdot q^4$ to the limiting length-scale ($q \to 2\pi/l_2$) following Porod's definition (Eq. (18)) and by changing the limit to π/r_0. Mathematically this can be expressed as

$$\begin{aligned}\sigma_{SF} &= \frac{1}{2\pi\phi(\Delta\rho)^2}\lim_{q\to\pi/r_0} I(q)\cdot q^4 \\ &= \frac{v_{pp}}{2\pi}\lim_{q\to\pi/r_0}(S(q)-1)\cdot q^4 \\ &= \frac{3\phi_b\Gamma(5-D_s)}{8r_0(2\pi)^{2-D_s}}\cdot\frac{\sin[\pi(3-D_s)/2]}{3-D_s}. \end{aligned} \quad (19)$$

Note that here we also assumed that the electron density of the aggregate is close to the electron density of the individual particles. However, when the electron density of the aggregate is substantially lower than that of the individual particles, due to a substantial contribution of electron lean regions between the bricks, the intensity of the structure factor will be reduced. Consequently, the obtained values for ϕ_b and σ_{SF} can be overestimated. Extrapolations of the surface fractal regimes are illustrated by the dashed portions of the lines in Figures 4(c) and 4(d). Please note that, although the scattering intensities in the low-q regime decrease, the actual extrapolation of this regime reveals increasing surface areas for increasing surface fractal dimensions. For example, as D_s increases from 2 to 3, while ϕ_b and r_0 are kept constant, the specific surface area σ_{SF} increases by a factor $\pi^2/2 \approx 4.9$. Moreover, the specific surface area is inversely proportional to r_0 as illustrated in Fig. 4(d). This holds for both the total specific surface of primary particles given by $\sigma_{pp} = 4\pi r_0^2/(4/3\,\pi r_0^3) = 3/r_0$ as well as for fractal rough aggregate surfaces as defined by Eq. (19).

Empirical validation of the surface fractal aggregate model

Above, we analytically derived properties of surface fractal aggregates (Eqs. (5), (16), and (17)) and demonstrated how this would work on a hypothetical system of spherical silica particles of a given density (Fig. 4). The profiles in the $\log I(q)$ *vs.* $\log q$ plots (Figs. 4(a) and 4(b)) showed that the inflection points in the scattering curves, separating the form factors and the structure factors, were a characteristic feature of the surface fractal aggregates. These inflection points and the associated intensity plateaus ($I(q) \propto q^0$) are related to the fact that only primary particles at the surface of the aggregates contribute to the low-q increase in intensity (see also Fig. 1(c)). We can empirically validate this observation by generating a Koch-like fractal surface aggregate representation composed of square-shaped primary particles (Fig. 5) and simulate *ab initio* their scattering pattern (see also supplementary material).

We validated our model by using a quadratic *von Koch* curve as described by Mandelbrot.[48] In such a case, the fractal generation involves a systematic surface roughening that has to be applied at varying length-scales of an initially square-shaped outline. However, contrary to the classical *von Koch* procedure, we simulated aggregates composed of smaller quadrilaterals of a similar size as the smallest segment of the outer aggregate contour line. This simple, yet elegant, approach allowed us to predict the morphology of an aggregate, which was model-independent because it does not rely on the mathematical definitions of the correlation function $g(r)$ described by Eq. (14). The generated aggregate object is akin to a "brick-in-a-wall" or mosaic structure, which exhibits a very dense packing of primary particles in agreement with the findings of Kolb and Herrmann.[25] In order for this to be valid, our hypothetical, computer-generated object had to be large enough to include all length-scales, in analogy to primary particles and the fractal rough surfaces of micron-sized aggregates (i.e., between 1 nm and 10 μm). Taking into account our limited computational capacities, we opted for a 2D instead of a 3D simulation approach. We found that simulating a 2D fractal contained within a matrix of 256×256 primary particles of an average size of 10×10 pixel^2 (Fig. 5) allowed us to evaluate all characteristic regions

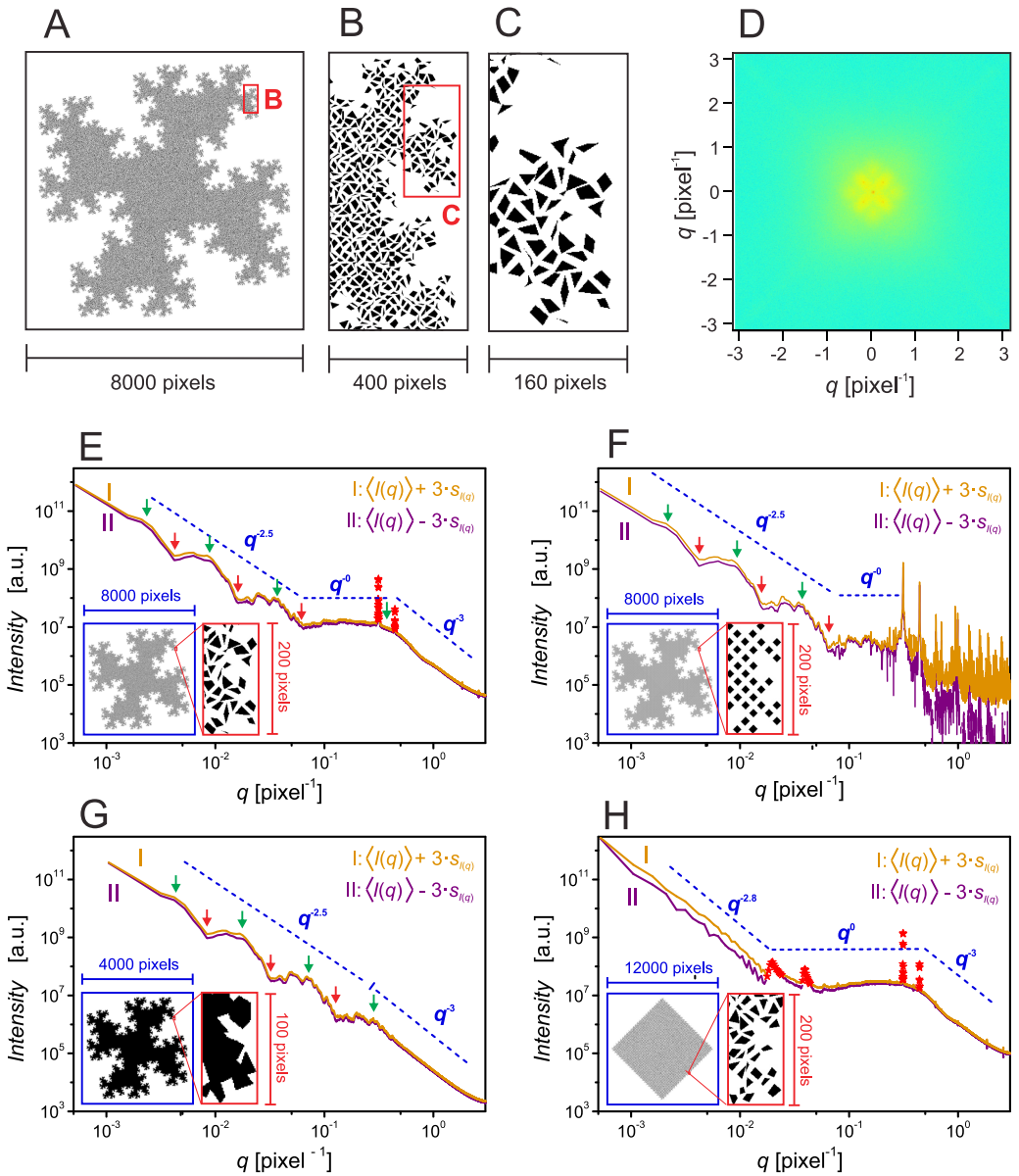

FIG. 5. Simulated contour *Koch*-like fractals composed of 2D square-shaped particles (black pixels) and their corresponding intensity patterns, with a contour fractal dimension of 1.5. (a) Real space 8000 × 8000 pixel^2 image of a contour fractal but rotated by 45° with 4 contour fractal iteration levels composed of 2^{16} quadrilaterals. The randomised square edge length is 2–20 pixels with the randomised inter-quadrilateral distances of 2–8 pixels (white pixels). In total 2^{18} quadrilateral edges, out of which 2^{14} edges are located at the outer boundary ($\phi_L = 6.25\%$); (b) and (c), respectively, 10× (image 800 × 400 pixel^2) and 40× (200 × 100 pixel^2) magnification of a contour fractal region in (a); (d) the square of the modulus of the 2D Fourier transform of the image in (a). Intensity scale increases: blue (lowest)-green-yellow-orange-red (highest); (e)-(h) azimuthally averaged intensity pattern for 4 different types of surface fractals, where the purple and orange line represent, respectively, the lower and higher boundary of a 99% confidence interval of 10 individually randomized contour fractals at 10 varying clockwise rotation angles in a range between 0° and 84°, with (e) azimuthally averaged intensity pattern of (a) (inlet represents 45° rotated contour fractal); (f) azimuthally averaged intensity pattern from a contour fractal as in (a), however with regular square-shaped bricks of 10 × 10 pixels and 10 pixel spacers. The input image is 8000 × 8000 pixel^2 (blue box) and the magnified images are 200 × 100 pixel^2 (red box); (g) azimuthally averaged intensity pattern from a contour fractal as in (a), but without the "low electron density" spacers, i.e., a dense fractal. The input image is 4000 × 4000 pixel^2 (blue box) and the magnified images are 100 × 50 pixel^2 (red box); (h) azimuthally averaged intensity pattern from a contour line fractal as in (a), but the aggregate contained 2 iteration levels, which are repeated 24× along the 4 aggregate edges. This routine results in a contour fractal with a larger number of squares as in (a) (9×2^{16}), but with a reduced number of edges at the outer boundary (3×2^{11}) leading to a reduced $\phi_L = 1.04\%$ as compared to a larger $\phi_L = 6.25\%$ of the surface fractal as shown in (a)-(e) (inlet surface fractal is 12 000 × 12 000 pixels (blue box) and zoom is 200 × 100 pixels (red box). In (e)-(h) the blue dashed lines mark the characteristic exponents of intensity scaling at different q-regimes. Moreover, green and red arrows indicate ((e)-(g)) the positions of bumps and dips in the scattering curves, respectively, which correlate with the self-similar build-up of surface fractal roughness pattern.

qualitatively, including the primary particle region, plateau region, and surface fractal region.

It is worth noting that working in 2D merely changed the considered definitions because we did not produce a fractal surface, but a fractal contour (as in Figs. 1(b) and 1(c)). Furthermore, scattering patterns from such 2D objects are expected to have exponents between −2 and −3 (rather than −3 and −4). We simulated four different contour fractals (Fig. 5) with a theoretical contour fractal dimension of $\log_4 8 = 1.5$, which should result in $I(q) \propto q^{-2.5}$. We started by building a contour fractal composed of 2^{16} quadrilaterals (i.e., primary particles, "bricks") with a randomized area between

4 and 200 pixels/quadrilateral (schematics in Figs. 5(a)-5(c)). Each black pixel represents a "high electron density" area. In order to suppress the potential symmetry contributions to the scattering patterns (see below), we randomized the positions of the quadrilaterals' vertices. Although each quadrilateral should have four edges, due to the randomization, some angles were either 0° or 180°, and thus some primary particles became triangular or line-shaped. The quadrilaterals were separated by white gaps in a range between 2 and 8 pixels, which represented the "low electron density" matrix. We assumed that the electron density of the electron-lean regions between the bricks equalled the electron density of the "solvent" surrounding an aggregate.

Then the 2D scattering intensity pattern is the square of the modulus of the 2D Fourier transform of the 2D image of an aggregate (Fig. 5(d)). This simulated pattern was in turn azimuthally averaged to a 1D scattering curve (Fig. 5(e)). This showed that the curve was qualitatively very similar to the scattering intensity patterns simulated with Eqs. (5), (15), and (17) (Figs. 4(a) and 4(c)). The simulation-derived intensity curve shown in Fig. 5(e) contains the three characteristic regions previously discussed: (I) low$-q$ surface fractal region ($0.0025 < q < 0.068$ pixel^{-1}, with $I(q) \propto q^{-2.5}$), (II) an inflection point and a plateau region ($0.068 < q < 0.30$ pixel^{-1}, with $I(q) \propto q^{0}$), and (III) a high-q form factor region ($0.45 < q < 3$ pixel^{-1}, with $I(q) \propto q^{-3}$). Despite the randomized distances between the neighbouring quadrilaterals, the intensity curve still contains suppressed correlation peaks, which correspond to the interparticle distances along the (1,0) and (1,1) directions with a d-spacing of 20 and 14.1 pixels, respectively (as shown by the red stars in Fig. 5(e)). Further randomization would be required to suppress these correlation peaks even more. Without this randomization, i.e., for an ordered arrangement of equally shaped squares, much stronger correlations/diffraction peaks are produced (Fig. 5(f)). Complete suppression, regardless of randomization, is practically impossible due to the algorithms used for the generation of the *Koch*-type contour fractal (see supplementary material).

In the simulated intensity patterns in Fig. 5, the length of the plateau regions depends on the fraction of quadrilateral edges at the outer boundary with respect to the total number of quadrilateral edges, ϕ_L. The fraction, ϕ_L, in these is a two-dimensional equivalent of the ϕ_b parameter that we introduced for the three-dimensional structure function in Eq. (16). We calculated the theoretical value of ϕ_L as follows: each quadrilateral was set to have essentially 4 edges, and the aggregate shown in Fig. 5(e) has thus a total of 2^{18} edges. Out of these 2^{14} were located at the outer boundary of the aggregate. This corresponds to a fraction of quadrilateral's edges at the boundary, $\phi_L = 6.25\%$. Therefore, the scaling constant of the structure factor was reduced to 6.25% with respect to the form factor's scaling constant, and as a result we observed an intermediate plateau region (Fig. 5(e)). Furthermore, the composition of the electron lean region in between the bricks can be different from the "solvent" that surrounds the whole aggregate. In such a case the system is composed of three distinct phases with different electron densities, namely, the electron density of the bricks (ρ_b), of the internal voids (ρ_{iv}), and of the surrounding solvent (ρ_{ss}). For increasing ρ_{iv} with respect to ρ_{ss}, the inner contrast ($\rho_b - \rho_{iv}$) will reduce with respect to the outer contrast ($\rho_b - \rho_{ss}$) (see Eq. (5)). Consequently, the outer edges contribute more than the inner edges. Therefore the apparent ϕ_L or ϕ_b values will increase for increasing electron density difference between internal voids and surrounding solvent ($\rho_{iv} - \rho_{ss}$). Unless the electron densities of the three phases are known we cannot unambiguously distinguish between an increase in ($\rho_{iv} - \rho_{ss}$) or ϕ.

Alternatively, when electron dense phases are merged together and the inner edges of the quadrilateral primary particles disappeared, we only observed a contrast difference at the outer contour line (Fig. 5(g)). The length of the q-range of the plateau region ($0.13 < q < 0.25$ pixel^{-1}) clearly decreased in size; however, it was not fully diminished, and the presence of this plateau region was very consistent over 10 different simulations. Nevertheless, this apparent plateau belongs to a sequence of bumps and dips (green and red arrows in Fig. 5(g)), which are separated from each other by a factor 4. A similar sequence of bumps and dips was observed for the "brick-in-a-wall" contour fractals (green and red arrows in Figs. 5(e) and 5(f)) and deterministic mass fractals as reported previously.[6,7] The fourfold ratio between the dips correlates with the fourfold ratio between the self-similar patterns of surface fractal roughness at different length-scales or iteration levels. Thus, the apparent plateau in Fig. 5(g) is an artefact that relates to the self-similar nature of rough fractal surfaces. Our simulation shows that the plateau region practically disappears for dense fractals (Fig. 5(g)) and is only observed when electron dense primary entities remain separated by electron lean regions, as "bricks-in-a-wall."

In order to validate the relation between surface fractal intensity scaling with the number of particles at the outer boundary, we reduced the relative number of primary quadrilaterals at the outer surface (Fig. 5(h)). This leads to 3×2^{11} of the quadrilaterals' edges from a total of 9×2^{16} edges to be located at the outer contour line yielding a ϕ_L value of 1.04%. As expected, the intensity of the low-q contour fractal regime further decreased with respect to the intensity of the surface fractal shown in Fig. 5(e), and the plateau region became expanded in the q-range. In overall, our *ab initio* approach confirmed that the intensity of the fractal region scaled proportionally with the number of primary entities at the aggregate's surface.

In the final part of this paper we apply the above-derived surface fractal concepts to real scattering data from a previous experimental work.[28] In our *in situ* and real-time scattering data on the nucleation and growth of $CaSO_4$ solids from supersaturated aqueous solution, we observed very characteristic surface fractal morphologies. These data sets were the initial inspiration to draft the surface fractal aggregate concept, which we now expanded and formalized in this work. In Fig. 6, we show a typical *in situ* small-angle X-ray scattering curve obtained from a 75 mmol/l $CaSO_4$ supersaturated solution after 150 s at 21 °C. In contrast to the assumptions made in our derivation, for the case of the experimental $CaSO_4$ data, the primary particles were found not to be spherical, but rather cylindrical in shape.[28] Thus, to fit the

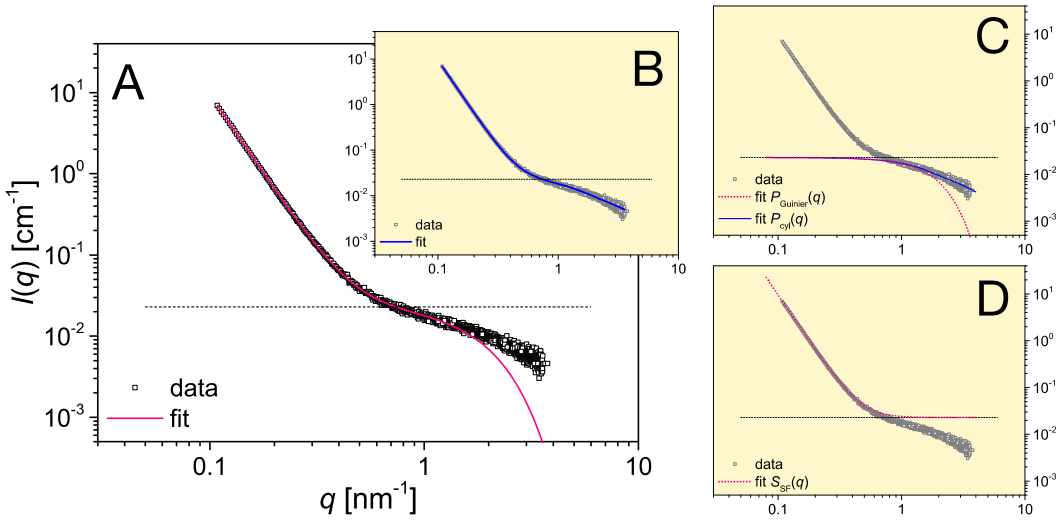

FIG. 6. *In situ* SAXS (Small Angle X-ray Scattering) curve from the solid phase forming in a 75 mmol/l $CaSO_4$ solution at 150 s (21 °C). Full experimental description of the measurement can be found elsewhere.[28] Fit parameters for (a)-(d) are based on Eqs. (5), (15), and (20) and using a cylindrical form factor with the main parameters expressed as $v_{pp}\phi(\Delta\rho)^2 = 0.022\,89\ cm^{-1}$, $R = 0.243$ nm, $L = 3.25$ nm, $R_{pp,g} = 0.953$ nm, $r_0 = 1.23$ nm, $D_s = 2.129$, $\phi_b = 0.100\,85$. The horizontal dashed line in all the panels corresponds to the intensity equal to the scattering pre-factor from Eq. (5), $v_{pp}\phi(\Delta\rho)^2$. (a) Best fit of the data based on Eqs. (5) and (16) ($S_{SF}(q)$) and Eq. (20) ($P_{Guinier}(q)$); (b) best fit of the data based on Eqs. (5) and (15), but by using a cylindrical form factor (variables R and L)[42] instead of the Guinier approximation from Eq. (20). $R_{pp,g}$ in the Guinier approximation is equal to the radius of gyration of a cylinder;[39] (c) comparison between the cylindrical form factor and the Guinier approximation and their extrapolation to $q \to 0$. Both form factors correspond to the same $R_{pp,g}$, and their profiles are identical for $q < \sim 2\ nm^{-1}$; (d) extrapolation of $S_{SF}(q)$ from Eq. (15) to $q \to \infty$ with r_0 parameter in the structure factor calculated from $R_{pp,g}$ of the form factor, under the assumption that the primary particles were spherical (meaning that they could be characterised by a single parameter r_0).

scattering curves at high-q, we exchanged the spherical for a cylindrical form factor,[40] which is a function of the particle length L and the cross-sectional radius R. This approach provides a more accurate description of the experimental data at high q-values, which contains information about the shape of the primary particles. However, deriving $S_{SF}(q)$ from Eq. (15) revealed that the position of the inflection point between $P(q)$ and $S(q)$ was dependent both on r_0, which is assumed to be the radius of a primary spherical particle, and on the fraction, ϕ_b, of these primary particles at the surface of the aggregate. Consequently, r_0 has to be known to evaluate correctly the fraction of the primary particles at the surface. Clearly, for spherical particles this is not an issue. On the other hand, for the cylindrical $CaSO_4$ primary particles, r_0 can be approximated by equating the radius of gyration $R_{pp,g}$ of a sphere to that of a cylinder. The solid red line in Fig. 6(a) represents the best fit to the data using Eq. (5). The surface fractal structure factor, $S_{SF}(q)$, was expressed by Eq. (15), and for the form factor we used the shape-independent Guinier approximation (Eq. (20)), where $R_{pp,g}$ is the radius of gyration for a primary particle (not the whole aggregate). In Fig. 6(b) we show a fit which includes a cylindrical form factor,

$$P_{\text{Guinier}}(q) = \exp\left(-\frac{q^2 R_{pp,g}2}{3}\right). \tag{20}$$

Although such a procedure affects the fit in the high-q part of the plot (at $q > 2\ nm^{-1}$ see Fig. 6(c)), it does correctly determine the position of the inflection point, because by definition $S(q \to \infty) = 1$ and $P_{\text{Guinier}}(q \to 0) = 1$. Therefore, regardless of the form factor contribution, the intensity corresponding to the inflection point becomes equal to the scattering pre-factor $v_{pp}\phi(\Delta\rho)^2$ introduced in Eq. (5), and shown in Fig. 6 by the dotted horizontal lines, which marks this intensity value. Consequently, the extrapolation of the structure factor from Eq. (15) to $q \to \infty$ (Fig. 6(d)) and the form factor from Eq. (20) to $q \to 0$ (Fig. 6(c)) mutually determines the $v_{pp}\phi(\Delta\rho)^2$ level and the q-coordinate inflection point. For the computer-generated *Koch*-like contour fractals, we demonstrated above (Figs. 5(e) and 5(g)) that the very occurrence of an inflection point and a plateau in the scattering region originates from a "low electron density" region separating the primary particles within an aggregate (compare Figs. 5(e) and 5(g)). Indeed, based on similar arguments we had previously concluded that the $CaSO_4$ surface fractal aggregates in our system were composed of anhydrous-$CaSO_4$ rod-shaped primary species in a water matrix. These are akin to high electron density "bricks" separated by lower electron density voids, i.e., a textbook example of a "brick-in-a-wall" structure. Using the above formulated surface structure factor fractal model we could thus show (Fig. 6) that indeed the precursor phase in the $CaSO_4$ system is made of such "brick-in-a-wall" structures.

CONCLUSIONS

We derived and validated a model for a structure factor expressed by Eq. (15) which describes the scattering from "brick-in-a-wall" surface fractal aggregates build of primary particles. We showed that scattering patterns from such structures exhibit three characteristic intensity scaling regions: (I) a low-q part yielding high scattering intensities with the intensity scaling proportional to q^{-6+D_s}, and which is described by a structure factor equation; (II) a high-q part representing only the scattering from the form factor of primary particles building the aggregate, and (III) the mid-q inflection point and a plateau ($I(q) \propto q^0$) separating regions I and II. The very

existence of such a plateau shows that within the aggregates, individual primary particles are distinguishable entities (as shown in Figs. 1(c) and 5(a)-5(c)). Such a distinction is achieved by introducing gaps in between the primary particles. These gaps can represent either a local disorder in the alignment of building blocks caused by the polydisperse nature of the shape and size of the primary particles or the presence of solvent rich, possibly diffuse, layers in between particles that do not contribute to the scattering contrast such as the crystal water. This arrangement is akin to a typical "brick-in-a-wall" arrangement, which is consistent with the concept of a mesocrystal[29] frequently observed as the outcome of non-classical crystal nucleation and growth processes.

SUPPLEMENTARY MATERIAL

See supplementary material for the algorithm we used for the generation of the *Koch*-type contour fractal.

ACKNOWLEDGMENTS

This work was partially supported by a Marie Curie grant from the European Commission in the framework of the MINSC ITN (Initial Training Research network), Project No. 290040. We thank Diamond Light Source for access to beamline I22 that contributed to the results presented here. A. J. Smith and N. J. Terrill are thanked for their competent support and advice. R.B., T.M.S., and L.G.B. acknowledge the financial support of the Helmholtz Recruiting Initiative.

[1]H. D. Bale and P. W. Schmidt, Phys. Rev. Lett. **53**, 596 (1984).
[2]M. H. Reich, S. P. Russo, I. K. Snook, and H. K. Wagenfeld, J. Colloid Interface Sci. **135**, 353 (1990).
[3]P. Wong and A. J. Bray, J. Appl. Crystallogr. **21**, 786 (1988).
[4]P. Wong and A. Bray, Phys. Rev. Lett. **60**, 1344 (1988).
[5]P. Wong and Q. Cao, Phys. Rev. B **45**, 7627 (1992).
[6]A. Y. Cherny, E. M. Anitas, V. A. Osipov, and A. I. Kuklin, Phys. Rev. E: Stat., Nonlinear, Soft Matter Phys. **84**, 1 (2011).
[7]P. W. Schmidt and X. Dacai, Phys. Rev. A **33**, 560 (1986).
[8]S. K. Sinha, T. Freltoft, and J. Kjems, Kinet. Aggregation Gelation **19842**, 87 (1984).
[9]T. Freltoft, J. K. Kjems, and S. K. Sinha, Phys. Rev. B **33**, 269 (1986).
[10]S.-H. Chen and J. Teixeira, Phys. Rev. Lett. **57**, 2583 (1986).
[11]J. Teixeira, J. Appl. Crystallogr. **21**, 781 (1988).
[12]J. Teixeira, Ferroelectrics **235**, 231 (1999).
[13]K. D. Keefer and D. W. Schaefer, Phys. Rev. Lett. **56**, 2376 (1986).
[14]D. W. Schaefer and K. D. Keefer, Phys. Rev. Lett. **56**, 2199 (1986).
[15]P. Meakin, Annu. Rev. Phys. Chem. **39**, 237 (1988).
[16]M. Y. Lin, H. M. Lindsay, D. A. Weitz, R. Klein, R. C. Ball, and P. Meakin, J. Phys.: Condens. Matter **2**, 5283 (2002).
[17]C. Oh and C. M. Sorensen, J. Aerosol Sci. **28**, 937 (1997).
[18]C. M. Sorensen and G. M. Wang, Phys. Rev. E: Stat. Phys., Plasmas, Fluids, Relat. Interdiscip. Top. **60**, 7143 (1999).
[19]R. C. Ball, D. A. Weitz, T. A. Witten, and F. Leyvraz, Phys. Rev. Lett. **58**, 274 (1987).
[20]P. van Dongen and M. Ernst, Phys. Rev. Lett. **54**, 1396 (1985).
[21]F. Pierce, C. M. Sorensen, and A. Chakrabarti, Phys. Rev. E: Stat., Nonlinear, Soft Matter Phys. **74**, 1 (2006).
[22]B. Mandelbrot, Science **156**, 636 (1967).
[23]T. Koga, T. Hashimoto, M. Takenaka, K. Aizawa, N. Amino, M. Nakamura, D. Yamaguchi, and S. Koizumi, Macromolecules **41**, 453 (2008).
[24]M. K. Ridley, V. A. Hackley, and M. L. Machesky, Langmuir **22**, 10972 (2006).
[25]M. Kolb and H. J. Herrmann, Phys. Rev. Lett. **59**, 454 (1987).
[26]J. F. Lutsko and G. Nicolis, Phys. Rev. Lett. **96**, 46102 (2006).
[27]J. F. Lutsko, J. Chem. Phys. **136**, 34509 (2012).
[28]T. M. Stawski, A. E. S. van Driessche, M. Ossorio, J. Diego Rodriguez-Blanco, R. Besselink, and L. G. Benning, Nat. Commun. **7**, 11177 (2016).
[29]M. Niederberger and H. Cölfen, Phys. Chem. Chem. Phys. **8**, 3271 (2006).
[30]F. Nindiyasari, L. Fernández-Díaz, E. Griesshaber, J. M. Astilleros, N. Sánchez-Pastor, and W. W. Schmahl, Cryst. Growth Des. **14**, 1531 (2014).
[31]B. Pokroy, L. Kabalah-Amitai, I. Polishchuk, R. T. Devol, A. Z. Blonsky, C. Y. Sun, M. A. Marcus, A. Scholl, and P. U. P. A. Gilbert, Chem. Mater. **27**, 6516 (2015).
[32]C. S. Frazer, E. C. Dickey, and A. Sayir, J. Cryst. Growth **233**, 187 (2001).
[33]R. L. Owen and E. Garman, Acta Crystallogr., Sect. D: Biol. Crystallogr. **61**, 130 (2005).
[34]R. A. Gosavi, V. Bhamidi, S. Varanasi, and C. A. Schall, Langmuir **25**, 4579 (2009).
[35]A. J. Malkin, Y. G. Kuznetsov, and A. McPherson, J. Struct. Biol. **117**, 124 (1996).
[36]J. Blanchard, F. Ribot, C. Sanchez, P.-V. Bellot, and A. Trokiner, J. Non-Cryst. Solids **265**, 83 (2000).
[37]C. M. Sorensen, Aerosol Sci. Technol. **35**, 648 (2001).
[38]C. M. Sorensen, J. Cai, and N. Lu, Langmuir **8**, 2064 (1992).
[39]L. A. Feigin and D. I. Svergun, "Structure Analysis by Small-Angle X-ray and Neutron Scattering" (Plenum Press, New York, 1987).
[40]A. Guinier and G. Fournet, *Small Angle Scattering of X-Rays* (John Wiley and Sons Inc., New York, 1955).
[41]P. Debye, R. Anderson, and H. Brumberger, J. Appl. Phys. **28**, 679 (1957).
[42]J. S. Pedersen, Adv. Colloid Interface Sci. **70**, 171 (1997).
[43]P. Pfeifer, D. Avnir, and D. Farin, J. Stat. Phys. **36**, 699 (1984).
[44]L. Körösi, S. Papp, I. Bertóti, and I. Dékány, Chem. Mater. **19**, 4811 (2007).
[45]A. Montesinos-Castellanos, E. Lima, J. A. de los Reyes H, and V. Lara, J. Phys. Chem. C **111**, 13898 (2007).
[46]W. M. Haynes, *CRC Handbook of Chemistry and Physics*, 92nd ed. (CRC Press, 2011).
[47]G. Porod, in *Small Angle X-Ray Scattering*, edited by O. Glatter and O. Kratky (Academic Press London Ltd., New York, 1982), pp. 17–51.
[48]B. Mandelbrot, in *Fractal Geometry of Nature*, 2nd ed., edited by B. Mandelbrot (W. H. Freeman and Co., New York, 1982), pp. 34–57.